Characterization and adaptive optical correction of aberrations during in vivo imaging in the mouse cortex

Na Ji[a,1], Takashi R. Sato[a,b], and Eric Betzig[a]

[a]Howard Hughes Medical Institute, Janelia Farm Research Campus, Ashburn, VA 20147; and [b]Werner Reichardt Centre for Integrative Neuroscience, University of Tübingen, 72076 Tübingen, Germany

The signal and resolution during in vivo imaging of the mouse brain is limited by sample-induced optical aberrations. We find that, although the optical aberrations can vary across the sample and increase in magnitude with depth, they remain stable for hours. As a result, two-photon adaptive optics can recover diffraction-limited performance to depths of 450 μm and improve imaging quality over fields of view of hundreds of microns. Adaptive optical correction yielded fivefold signal enhancement for small neuronal structures and a threefold increase in axial resolution. The corrections allowed us to detect smaller neuronal structures at greater contrast and also improve the signal-to-noise ratio during functional Ca²⁺ imaging in single neurons.

The ability to visualize biological systems in vivo has been a major attraction of optical microscopy, because studying biological systems as they evolve in their natural, physiological state provides relevant information that in vitro preparations often do not allow (1). However, for conventional optical microscopes to achieve their optimal, diffraction-limited resolution, the specimen needs to have identical optical properties to those of the immersion media for which the microscope objective is designed. For example, one of the most widely applied microscopy techniques for in vivo imaging, two-photon fluorescence microscopy, often uses water-dipping objectives. Because biological samples are comprised of structures (i.e., proteins, nuclear acids, and lipids) with refractive indices different from that of water, they induce optical aberrations to the incoming excitation wave and result in an enlarged focal spot within the sample and a concomitant deterioration of signal and resolution (2, 3). As a result, the resolution and contrast of optical microscopes is compromised in vivo, especially deep in tissue.

Many questions related to how the brain processes information on both the neuronal circuit level and the cell biological level can be addressed by observing the morphology and activity of neurons inside a living and, preferably, awake and behaving mouse (1). In a typical experiment, an area of the skull is surgically removed and replaced with a cover glass to provide optical access to the underlying structure of interest (4). For imaging during behavior, the cover glass is often attached to an optically transparent plug embedded in the skull to improve mechanical stability and to prevent the skull from growing back and blocking the optical access (5, 6) (Fig. 1A). Before the excitation light of a two-photon microscope reaches the desired focal plane inside the brain, it has to traverse first the cranial window and then the brain tissue, both with optical properties different from water. Thus, they both impart optical aberrations on the excitation light, which leads to a distorted focus, even at the surface of the brain.

These sample-induced aberrations can be corrected with adaptive optics (AO) to recover diffraction-limited resolution. In AO, a wavefront-shaping device modifies the phase of the excitation light before it enters the sample in such a way as to cancel out the phase errors induced by the sample (7). Originally developed for applications in astronomy, the most common AO setup uses a sensor to measure the wavefront after it passes through the aberrating medium (e.g., atmosphere in astronomical AO). This information is then used to control the wavefront-shaping device, which is usually a deformable mirror or a spatial light modulator (SLM) (8). However, this direct wavefront-sensing approach is not suitable for imaging in vivo. For one, it is not possible to place the wavefront sensor past the aberrating medium, which in this case would still be within the brain. Other approaches where the wavefront of the light reflected from the sample is directly measured are limited, because the strong scattering of light in brain tissue scrambles the information in the reflected wavefront (9, 10).

Recently, we developed an image-based AO approach that does not require direct wavefront measurement and that is insensitive to sample scattering (11). By comparing images of the sample taken with different segments of the pupil illuminated, the local slope of the wavefront is measured from image shift. The phase offset for each segment is then either measured directly via interference or calculated by using phase reconstruction algorithms similar to those developed for astronomical AO. This pupil-segmentation-based approach as applied to two-photon fluorescence microscopy can recover diffraction-limited performance in both biological and nonbiological samples, including fixed brain slices. The question remains, however, whether the same enhancements can be achieved during two-photon imaging in the intact mouse. Issues that must be addressed include how fast optical aberrations evolve in vivo, what the magnitude and complexity of their spatial variation are, and to what degree adaptive optical correction can improve both the signal and the resolution during morphological and/or functional imaging. Here we answer these questions and demonstrate that we can recover diffraction-limited resolution at a depth of 450 μm in the cortex of the living mouse.

Results and Discussion

Diffraction-Limited Resolution Can Be Recovered in Vivo by AO. Using fluorescent beads introduced into a mouse cortex by in utero electroporation (12), we can correct the optical aberrations induced by the cranial window and cortical tissue. For example, in Fig. 1 A–F, the signal is increased 3.3× at the same excitation power after AO correction when imaging a 2.0-μm-diameter red-emitting fluorescent bead 170 μm below the surface of the brain. The resulting resolution improvement on GFP-expressing dendritic branches is most significant in the axial direction, because axial resolution is more sensitive to the existence of aberration (11, 13). The improved signal and resolution result in substantially enhanced contrast, such that twice as many dendritic
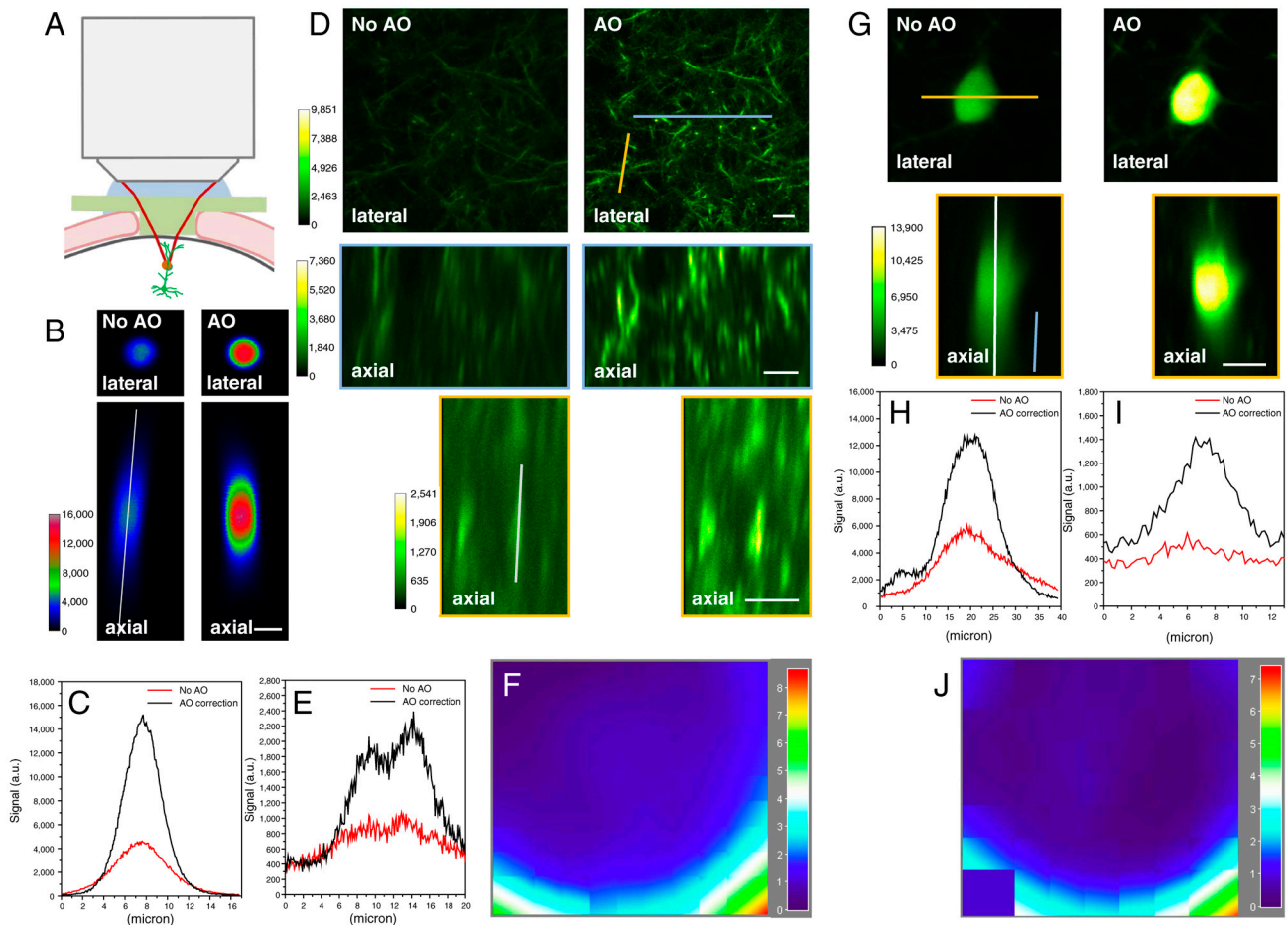
Fig. 1. AO improves imaging quality in vivo: (*A*) schematic of the geometry for in vivo imaging in the mouse brain, showing the cranial window (green) embedded in the skull (pink) to provide stability to the brain as well as optical access. (*B*) Lateral and axial images of a 2-μm-diameter bead 170 μm below the brain surface before and after AO correction. (*C*) Axial signal profiles along the white line in *B* before and after AO correction. (*D*) Lateral and axial images of GFP-expressing dendritic processes over a field centered on the bead in *A*. (*E*) Axial signal profiles along the white line in *D*. (*F*) Measured aberrated wavefront in units of excitation wavelength. (*G*) Lateral and axial images of GFP-expressing neurons 110 μm below the surface of the brain with and without AO correction. (*H*) Axial signal profiles along the white line in *G*. (*I*) Axial signal profiles along the blue line in *G*. (*J*) Aberrated wavefront measured in units of excitation wavelength. (Scale bars: 2 μm in *B* and 10 μm elsewhere.)

processes can be defined after correction than before (Fig. S1). For samples where photodamage and photobleaching increase with excitation power faster than does the two-photon signal (14), achieving diffraction-limited resolution in vivo would allow one to use lower excitation power and thus alleviate such undesired photoinduced effects.

In lieu of fluorescent beads, somata of GFP-labeled neurons can also be used for AO correction. Fig. 1 *G* and *H* shows an example correction, with substantially improved axial resolution, a 2× signal gain at the soma, and 5× gain at a nearby dendrite (Fig. 1*I*). As a general rule, smaller structures show larger signal gain upon AO correction than larger structures: The enlarged focal volume caused by aberration allows more fluorophores to be excited in a large fluorescent structure like a soma, thus partly compensating for the decreased focal intensity; for small fluorescent features such as micron-sized beads and dendrites, the full impact of reduced focal intensity is felt more acutely. This phenomenon is further highlighted in Fig. S2, where correcting aberrations introduced by a cranial window yields an almost 5.8× signal increase for a 0.5-μm bead, 3.8× increase for a 2-μm bead, and 1.8× signal increase for a fluorescent sea sample.

Brain-Induced Aberrations Are Temporally Stable over Hours. The temporal stability of brain-induced aberrations is a critical factor determining the practical application of AO in vivo. In astrono-my, rapid fluctuations in the atmosphere require AO corrections on the millisecond scale (8). Our measurements (Fig. 2) show that in vivo aberrations in the mouse cortex are stable for several hours, which allows us to use pupil segmentation algorithms even with relatively slow wavefront-shaping devices such as an SLM. Indeed, for the cases of bead correction at depths of 60 and 90 μm in Fig. 2, the wavefront change over 1–2 h is only 0.05 and 0.08 waves rms, respectively. We note that this result applies to corrections over 100 pupil segments, which is sufficient to handle the aberration modes (e.g., spherical aberration, coma, astigmatism, etc.) normally associated with adaptive optics. With a much larger number of pupil regions, such as would be required to compensate for scattering by high spatial frequency inhomogeneities in the tissue, faster methods may be needed (15).

Brain-Induced Aberrations Increase with Imaging Depth. It is a common observation that image resolution and contrast degrade with imaging depth. Using 2-μm fluorescent beads introduced into the cortex by in utero electroporation, we compared sample-induced aberrations at different depths quantitatively (16). In Fig. 3, we summarize the axial full width at half maximum (FWHM) and fluorescence intensity of these beads at depths down to 400 μm under three conditions: without AO correction, with AO correction for the cranial window only, and with full AO correction for both the cranial window and cortex tissue. We also show the

Ji et al.

www.manaraa.com
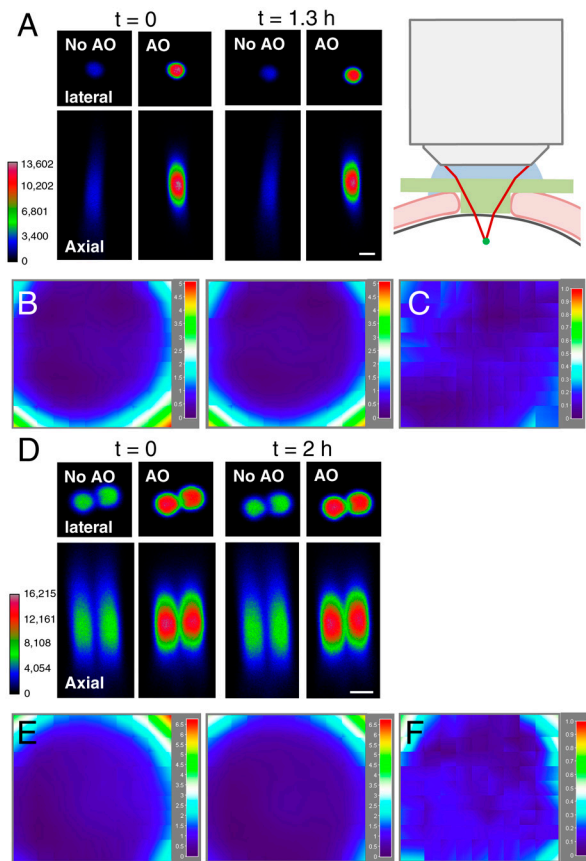
Fig. 2. Brain-induced aberrations are temporally stable over hours: (*A*) Lateral and axial images of a 2-μm-diameter bead 60 μm below the surface of the brain before and after AO correction, measured 1.3 h apart. (*B*) Aberrated wavefronts measured at the two times in *A*, in units of excitation wavelength. (*C*) Difference between the aberrated wavefronts in *B*, in units of excitation wavelength (note the smaller magnitude scale than in *B*). (*D*) Lateral and axial images of a pair of 2-μm beads 90 μm below the surface of the brain before and after AO correction, measured 2 h apart. (*E*) Aberrated wavefronts measured at the two times in *D*, in units of excitation wavelength. (*F*) Difference between the aberrated wavefronts in *E*, in units of excitation wavelength (note the smaller magnitude scale than in *E*). (Scale bar: 2 μm.)

rms wavefront error for the brain-induced component of the aberration. The expected aberration increase with image depth is indeed observed. Cranial window correction improves imaging performance at all depths, but full AO correction of both the window and the tissue is needed to recover optimal diffraction-limited performance beyond 100 μm. The maximal signal and axial resolution improvements are 7.5× and 3×, respectively. The images of the beads before and after AO correction, as well as the aberrated wavefront, are shown in Fig. S3. In the above data, we measured the optical aberrations after moving the beads to the center of the scanning field of view, so that the excitation light always passes through the cranial window in the identical path and thus experiences identical aberration from the cranial window. When we did not adjust the sample position, but rather measured the aberrations at both different depths and different scanning-field positions, we still observed similar trends down to 450 μm in vivo (Fig. S4).

The Spatial Variation of Sample-Induced Aberration Depends Highly on Tissue Structure. Because the mouse brain is optically inhomogeneous and because the excitation light travels through different tissue as the focus is scanned, the optical aberration is expected to vary at different focal positions. The variation with depth (Fig. 3) is described above. But to what extent can a single

AO correction at one point be applied to a larger surrounding volume? Its applicability depends on the magnitude and spatial scale of the inhomogeneities in the beam path, relative to the spatial scale of pupil segments used for correction. For example, in Fig. 4*A*, AO correction on a fluorescent bead at 65-μm depth improves the signal and axial resolution only for dendrites (e.g., the asterisk in Fig. 4*A*) within a few microns of the bead, due to the presence of a large blood vessel nearby (the dotted circle in Fig. 4*A*), which serves as a cylindrical lens to perturb the excitation light in a highly position-dependent manner. On the other hand, in regions devoid of such large aberrating bodies, an AO correction at a single point can improve imaging over a substantial volume. In Fig. 4*B*, for example, AO correction on a bead at 160-μm depth improves the signal and resolution over a $102 \times 102 \times 96 \ \mu m^3$ volume. Of course, as mentioned in the context of temporal stability, the greater the number of pupil regions and hence the greater the degree of correction at a single point, the more likely it is that the correction is valid over a smaller region in the vicinity of the correction point.
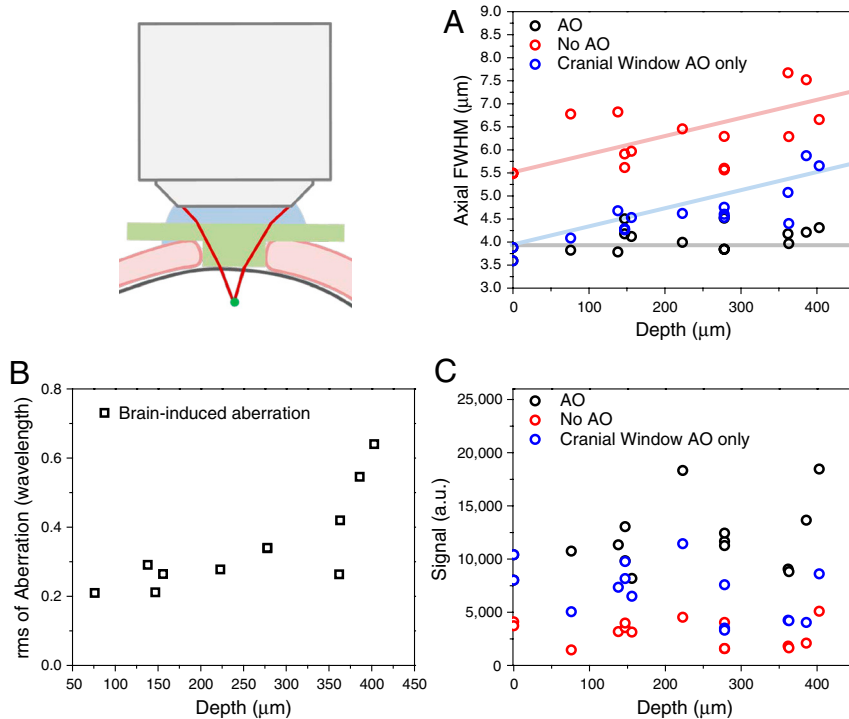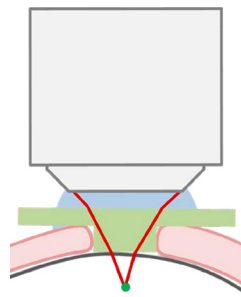
Correction for Cranial Window Aberration Alone Is Beneficial. Although the effect of brain-induced aberration becomes significant beyond 100 μm (Fig. 3), at more superficial depths, correction for the cranial window alone is sufficient to recover near diffraction-limited performance. For example, images of superficial dendritic structures transfected with cytosolic green calcium modulated protein (GCaMP3) with and without cranial window correction reveal superior signal and image resolution after correction (Fig. 4*C*; also see Movies S1 and S2). Compared to corrections on a fluorescent bead embedded inside the brain, cranial window correction applies over a larger volume than the locally specific correction due to brain tissue inhomogeneities (Fig. S5).

These results suggest three practical tips to improve imaging quality during in vivo two-photon fluorescence microscopy even without adaptive optics. First, minimizing the cranial window thickness or using a material with a refractive index similar to water (e.g., Teflon® fluorinated ethylene propylene or tetraethoxysilane) will reduce the magnitude of the window-induced aberration. On the other hand, a glass window also helps to stabilize the brain and inhibit regrowth of the skull in chronic experiments. Second, aligning the head of the mouse so that both the cranial window and the surface of the brain are perpendicular to the optical axis of the objective will reduce off-axis aberrations such as astigmatism or coma. Finally, underfilling the objective with excitation light could improve the image signal (Fig. S6) because of two factors: Underfilling causes more laser power to be transmitted through the objective, and the lower excitation numerical aperture (N.A.) caused by underfilling results in less aberration of the excitation, at least for the types of aberrations measured in mouse brain in vivo. Underfilling a high-N.A. objective is preferable to using a lower-N.A. objective, because the high-N.A. objective collects fluorescence signal more efficiently.

AO Correction Improves Calcium Imaging in Vivo. One important application of in vivo two-photon imaging in the brain is calcium imaging of neural activity. Fig. 5 shows examples of calcium imaging at 155-μm depth of neurons in layer 2/3 of the mouse primary visual cortex with and without AO correction for the cranial window. Similar to the GFP-labeled neuron of Fig. 1*G*, the basal fluorescence signal F from Oregon green 488 1,2-bis(2-aminophenoxy)ethane-*N,N,N′,N′*-tetraacetate-1, acetoxymethyl ester (OGB-1 AM) labeled soma is enhanced by AO correction. In addition, 30% of the neurons (SD = ±7%, eight imaging sessions, 107 neurons total) that respond to visual stimulation show increased baseline-normalized signal changes $\Delta F/F$. This increase is most likely caused by the reduction in focal volume after correction: If the original aberrated and thus enlarged focal volume extends beyond the soma into the surrounding neuropil, $\Delta F/F$

Fig. 3. Brain-induced aberrations increase with imaging depth: (*A*) The axial FWHMs of images of 2-μm-diameter beads at various depths down to 400 μm below the surface of brain, as measured without AO correction (red), with AO correction for the cranial window alone (blue), and with full AO correction for both the cranial window and the brain (black). The colored lines serve as guides to the eye, with the gray line denoting the diffraction-limited axial FWHM. (*B*) The rms magnitude of the brain-induced aberrated wavefront versus imaging depth, in units of excitation wavelength. (*C*) The signal from 2-μm beads under all three conditions.
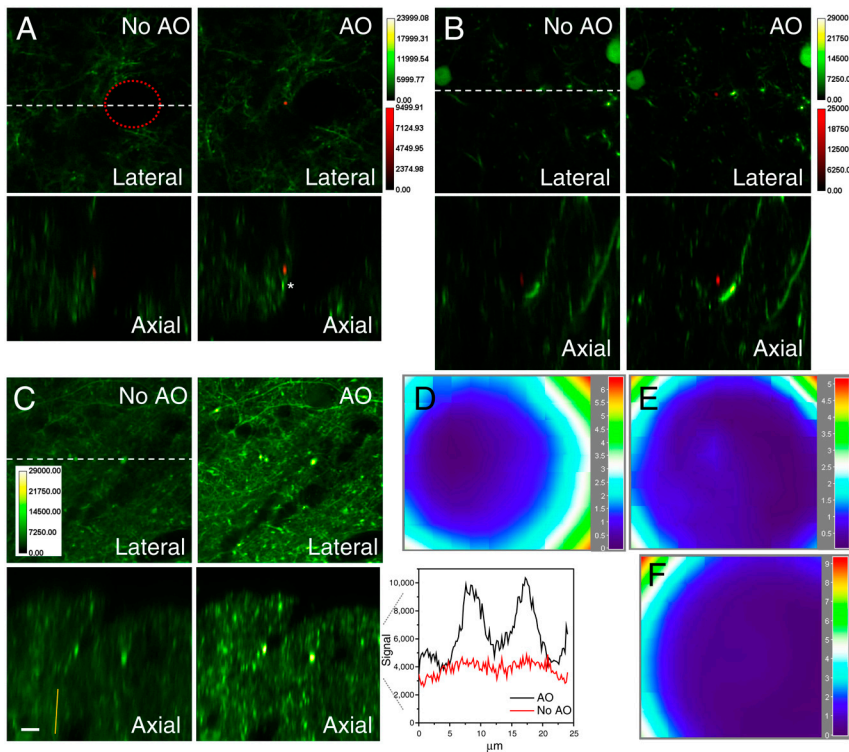
Fig. 4. Sample-induced aberrations depend highly on local tissue structure: (*A*) The AO correction on a 2-μm-diameter bead (red channel) at 65-μm depth improves the lateral and axial images of only nearby dendrites (green channel, white asterisk), because a neighboring capillary (red dashed circle) introduces a spatially localized aberration on the bead. (*B*) The AO correction on another 2-μm-diameter bead at 160-μm depth in a region of the brain without such large inhomogeneities improves imaging over a much larger volume. (*C*) AO correction for the cranial window alone is sufficient to recover diffraction-limited resolution at superficial depths (32 μm for the lateral images). The *Inset* to the right shows the axial signal profile along the orange line in *C*. (*D–F*) Aberrated wavefronts measured for *A–C*, respectively, in units of excitation wavelength. (Scale bar: 10 μm.)

Ji et al.

www.manaraa.com
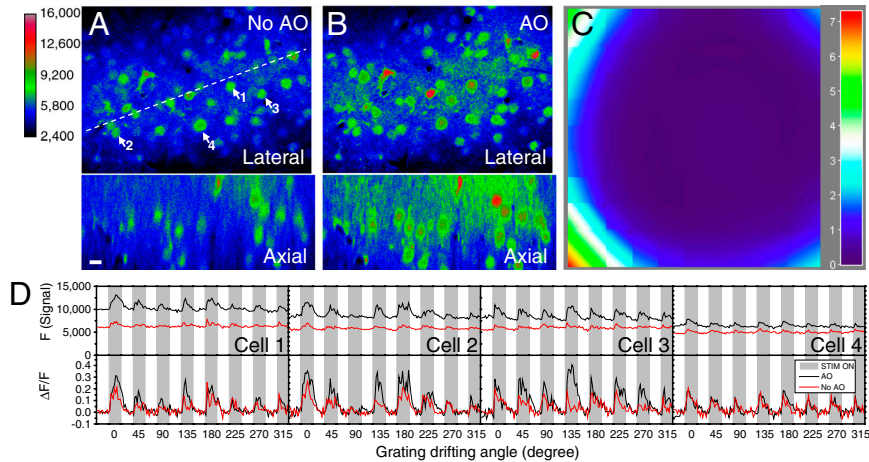
Fig. 5. AO correction improves calcium imaging in vivo. (*A*) Lateral and axial images of OGB-1 AM labeled neurons at 155 μm below the brain surface without AO correction. (*B*) Lateral and axial images of the same neurons with AO correction for the cranial window. (*C*) Measured aberrated wavefront in units of excitation wavelength. (*D*) Fluorescence signal (*Upper*) and its percentage change (*Lower*) for four cells indicated in *A* with and without AO correction. Gray bars denote the time periods during which black-and-white gratings drift in eight different directions at, from left to right, 0°, 45°, 90°, 135°, 180°, 225°, 270°, and 315°.

will be reduced by the uncorrelated fluorescence fluctuations in the tissue relative to the soma (17). Furthermore, 80% of the neurons exhibiting the largest visual responses (defined here as having $\Delta F/F > 20\%$) show an increase in $\Delta F/F$ upon AO correction (SD = ±20%, eight imaging sessions, 36 cells total). We speculate that these neurons are the ones whose somas straddle the focal plane, so that the reduction of focal volume upon correction most effectively rejects the neuropil contribution in these cases (18). The ability of AO to reduce the excitation volume at depth and improve the signal-to-noise ratio of Ca^{2+} imaging may prove especially beneficial for studying closely packed and densely labeled neuronal populations.

Summary. By incorporating AO in a two-photon fluorescence microscope, we demonstrate that the optical aberrations induced by brain tissue and/or a cranial window can be compensated in vivo to recover diffraction-limited performance at depth in the mouse brain. We observe signal and resolution gains during both morphological and functional imaging, with the largest improvements seen on small features such as fine dendritic processes. Indeed, with adaptive optics we can now image to >400 μm deep into the brain with resolution similar to that normally seen at the superficial depth in brain slices. As a result, adaptive optics would play an important role in the application of many physiological techniques in vivo, such as two-photon uncaging (19), two-photon imaging of dendrites, spines, and axons (20), multiphoton ablation of neuronal structures (21), optogenetic stimulation (22, 23), and superresolution imaging (24).

Materials and Methods

Instrumentation. Our custom adaptive optical two-photon fluorescence microscope has been described in detail previously (11). Briefly, we used two galvanometers to scan the laser focus in the *X* and *Y* directions (the objective axis being the *Z* direction). To keep the phase correction stationary during beam scanning, the *X* and *Y* galvanometers were conjugated to each other, and the *Y* galvanometer was conjugated to a phase-only SLM, which was then conjugated to the back pupil plane of a 16×, 0.8 N.A. objective. All the optical conjugation was achieved by custom-designed telecentric f-θ lenses. Laser light from a tunable Ti:sapphire laser was used to generate two-photon fluorescence, which was collected in the epidirection and separated into green and red channels to be detected by photomultiplier tubes. For green fluorescence protein and fluorescence bead imaging, 900-nm light was used for excitation. For OGB-1 AM imaging, 850 nm was used. During pupil segmentation, small areas of pupil were illuminated and the resulting images were analyzed to measure the image shifts. Before the galvanometers, a motorized 1–4× beam reducer (Special Optics, Inc.) was used to shrink the size of the excitation laser to fit the area of the SLM to be illuminated,

and a pair of mirrors mounted on rapid translational stages (PILine® Translation Stage; Physik Instrumente) were used to direct the excitation laser to the specific segment under investigation, in order to utilize the available laser power more efficiently. System aberrations introduced by the optical setup were compensated before all experiments; thus, all aberrations shown were caused by the samples themselves.

AO Correction. For all AO corrections, we used the overlapping mask approach for local wavefront slope measurement and phase reconstruction to obtain the phase offsets (11). Typically, we turn on a pupil segment with 1/25 of the full-pupil area but overlap successive segments by half of their dimension to generate 81 distinct segments. With one additional image taken with full-pupil illumination as the reference image, 82 images were used for AO measurement, which usually took around 1 min at an imaging rate of 1–4 Hz. To measure the cranial-window-induced aberrations, during the craniotomy procedure, we deposited 1–10 μL of 2-μm-diameter fluorescent beads suspended in artificial cerebral saline onto the surface of the brain before installing the cranial window. The beads lying between the cranial window and the dura were used for AO correction on the cranial window.

Visual Stimulation

Visual stimuli were controlled by custom-written software. The stimuli were black and white square-wave gratings at 30° viewing angle and 100% contrast drifting at 2 Hz in eight different orientations (0°, 45°, 90°, 135°, 180°, 225°, 270°, and 315°). The stimuli were presented as a sequence, composed of eight stimuli of different orientation (6–8 s for each stimulus, and the same duration for the black screen during interstimuli intervals). For each imaging session, the sequence was repeated 4–6 times.

Animal and Surgery Procedure. All experimental protocols were conducted according to the National Institutes of Health guidelines for animal research and were approved by the Institutional Animal Care and Use Committee at Janelia Farm Research Campus, Howard Hughes Medical Institute.

In Utero Surgeries. DNA and beads were injected into in utero embryonic mice brain to label layer II/III neurons (25). E15-E16 timed-pregnant mice were deeply anesthetized with an isoflurane-oxygen mixture (2% vol isoflurane/vol O_2). The uterine horns were exposed, and 0.5 μl of fluorescent beads in solution or a DNA-beads mixture (containing 0.5 μL 2 μg/μL of plasmid expressing green protein and 0.5 μl of fluorescent beads) was pressure injected through a pulled-glass capillary tube into the ventricle of each embryo. For the DNA-beads mixture, the head of each embryo was placed between custom-made tweezer electrodes, and electroporation was achieved with five square pulses

(duration = 50 ms, frequency = 1 Hz, 40 V). For injection of beads alone, the electrical pulses were not applied. In either case, beads were observed to be sparsely distributed in L2/3 at the time the experiments were performed.

Viral Infection. Adult mice were anesthetized with isoflurane (2% vol isoflurane/vol O_2). A small hole was drilled into the skull by using a dental drill. Then 20 nL of suspended adeno-associated virus–GCaMP3 virus (Penn Vector Core, http://www.med.upenn.edu/gtp/vectorcore/) was slowly introduced into the neocortex with a microinjector (26). The marginal skin was then closed up with suture. Imaging started at least 2 wk after viral infection.

Craniotomy. Mice were anesthetized by using an isoflurane-oxygen mixture (1–2% vol isoflurane/vol O_2). Body temperature was maintained at 37 °C by using a heating blanket. A head plate was glued to the skull, and a craniotomy (1.8–2 mm) was made over the cortex with the dura intact. A cranial window composed of a no. 1 cover glass and a 0.19–0.25 mm thick glass plug was placed over the craniotomy and then attached to the skull and the head plate by dental cement. Mice were then mounted under the adaptive optical two-photon microscope and kept anesthetized with isoflurane (1–1.5% vol isoflurane/vol O_2) during imaging.

Dye Loading. After mice were anesthetized with isoflurane (1% vol isoflurane/vol O_2), a head plate was glued to the skull, and a craniotomy (1.8–2 mm) was made over the primary visual cortex, leaving the dura intact. Dye solution [0.8 mM OGB-1 AM, 6% DMSO, 1.2% (wt/vol) pluronic acid, and 30 mM sulphur rhodamine 101 in Hepes-buffered artificial cerebral spine fluid (160 mM NaCl, 6 mM KCl, 13 mM glucose, 13 mM 4-(2-hydro-xyethyl)-1-piperazineethanesulfonic acid (Hepes), 2.5 mM $CaCl_2$, 2.5 mM $MgSO_4$)] was introduced by using a microinjector (Narishige, MO-10) at 200 μm below the dura. After dye injection, a cranial window composed of a no. 1 cover glass and a 0.19–0.25 mm thick glass plug was placed over the craniotomy and then glued to the skull and the head plate by using dental cement. Mice were then mounted under the adaptive optical two-photon microscope and kept anesthetized with isoflurane (1–1.5% vol isoflurane/vol O_2) for imaging under visual stimulation.

1. Kerr JND, Denk W (2008) Imaging *in vivo*: Watching the brain in action. *Nat Rev Neurosci* 9:195–205.
2. Schwertner M, Booth MJ, Neil MAA, Wilson T (2004) Measurement of specimen-induced aberrations of biological samples using phase stepping interferometry. *J Microsc* 213:11–19.
3. Schwertner M, Booth MJ, Wilson T (2004) Characterizing specimen induced aberrations for high NA adaptive optical microscopy. *Opt Express* 12:6540–6552.
4. Holtmaat A, et al. (2009) Long-term, high-resolution imaging in the mouse neocortex through a chronic cranial window. *Nat Protoc* 4:1128–1144.
5. Dombeck DA, Khabbaz AN, Collman F, Adelman TL, Tank DW (2007) Imaging large-scale neural activity with cellular resolution in awake, mobile mice. *Neuron* 56:43–57.
6. Komiyama T, et al. (2010) Learning-related fine-scale specificity imaged in motor cortex circuits of behaving mice. *Nature* 464:1182–1186.
7. Booth MJ (2007) Adaptive optics in microscopy. *Philos Trans R Soc Lond A* 365:2829–2843.
8. Hardy JW (1998) *Adaptive Optics for Astronomical Telescopes* (Oxford Univ Press, London).
9. Liang J, Williams DR, Miller DT (1997) Supernormal vision and high-resolution retinal imaging through adaptive optics. *J Opt Soc Am A* 14:2884–2892.
10. Rueckel M, Mack-Bucher JA, Denk W (2006) Adaptive wavefront correction in two-photon microscopy using coherence-gated wavefront sensing. *Proc Natl Acad Sci USA* 103:17137–17142.
11. Ji N, Milkie DE, Betzig E (2010) Adaptive optics via pupil segmentation for high-resolution imaging in biological tissues. *Nat Methods* 7:141–147.
12. Saito T (2006) In vivo electroporation in the embryonic mouse central nervous system. *Nat Protoc* 1:1552–1558.
13. Gibson SF, Lanni F (1991) Experimental test of an analytical model of aberration in an oil-immersion objective lens used in three-dimensional light microscopy. *J Opt Soc Am A* 8:1601–1613.
14. Ji N, Magee JC, Betzig E (2008) High-speed, low-photodamage nonlinear imaging using passive pulse splitters. *Nat Methods* 5:197–202.
15. Cui M, McDowell EJ, Yang C (2010) An *in vivo* study of turbidity suppression by optical phase conjugation (TSOPC) on rabbit ear. *Opt Express* 18:25–30.
16. Débarre D, et al. (2009) Image-based adaptive optics for two-photon microscopy. *Opt Lett* 34:2495–2497.
17. Kerr JND, Greenberg D, Helmchen F (2005) Imaging input and output of neocortical networks in vivo. *Proc Natl Acad Sci USA* 102:14063–14068.
18. Sato TR, Gray NW, Mainen ZF, Svoboda K (2007) The functional microarchitecture of the mouse barrel cortex. *PLoS Biol* 5:e189.
19. Noguchi J, et al. (2011) *In vivo* two-photon uncaging of glutamate revealing the structure-function relationships of dendritic spines in the neocortex of adult mice. *J Physiol* 589:2447–2457.
20. Jia H, Rochefort NL, Chen X, Konnerth A (2010) Dendritic organization of sensory input to cortical neurons *in vivo*. *Nature* 464:1307–1312.
21. Allegra Mascaro AL, Sacconi L, Pavone FS (2010) Multi-photon nanosurgery in live brain (Translated from English). *Front Neuroenergetics* 2:21.
22. Andrasfalvy BK, Zemelman BV, Tang J, Vaziri A (2010) Two-photon single-cell optogenetic control of neuronal activity by sculpted light. *Proc Natl Acad Sci USA* 107:11981–11986.
23. Papagiakoumou E, et al. (2010) Scanless two-photon excitation of channelrhodopsin-2. *Nat Methods* 7:848–854.
24. Ding JB, Takasaki KT, Sabatini BL (2009) Supraresolution imaging in brain slices using stimulated-emission depletion two-photon laser scanning microscopy. *Neuron* 63:429–437.
25. Saito T, Nakatsuji N (2001) Efficient gene transfer into the embryonic mouse brain using *in vivo* electroporation. *Dev Biol* 240:237–246.
26. Tian L, et al. (2009) Imaging neural activity in worms, flies and mice with improved GCaMP calcium indicators. *Nat Methods* 6:875–881.

www.manaraa.com